Journal Name

ARTICLE TYPE

Cite this: DOI: 00.0000/xxxxxxxxxx

Traction-separation laws of graphene grain boundaries†

Md. Imrul Reza Shishir,[a] and Alireza Tabarraei*[a]

Received Date
Accepted Date

DOI: 00.0000/xxxxxxxxxx

Molecular dynamics simulations are used to extract the traction–separation laws (TSLs) of symmetric grain boundaries of graphene. Grain boundaries with realistic atomic structures are constructed using different types of dislocations. The TSLs of grain boundaries are extracted by using cohesive zone volume elements (CZVEs) ahead of the crack tip. The traction and separation of each cohesive zone volume element are calculated during the crack growth. The traction and separation values obtained for the cohesive elements predict that the TSLs of grain boundaries have a bilinear form. The areas under the traction–separation curves are used to calculate the separation energy of the grain boundaries. The results show that as the grain boundary misorientation angle increases the separation energy of the grain boundaries decreases. The impact of temperature on the traction separation laws is studied. The results show that by increase of the temperature from 0.1 K to 300 K, the separation energy first increases to reach its peak at around 25 K and then slightly decreases.

1 Introduction

Graphene, a monolayer of carbon atoms packed together in a honeycomb lattice structure, has drawn remarkable attention due to its extraordinary properties which make it a suitable material for a wide range of technological applications[1–6]. Various techniques such as exfoliation[7], reduction of graphene oxide[8], sublimation of silicon carbide[9] and chemical vapor deposition (CVD)[10,11] have been proposed to produce or isolate graphene sheets. Among these techniques, CVD is the most widely used method for the creation of large graphene sheets. Graphene films prepared by chemical vapor deposition (CVD) are polycrystalline sheets composed of grains of varying orientation and size joined together by grain boundaries. Grain boundaries act as defects and alter the mechanical properties of graphene. It has been reported that pristine graphene is the strongest material with Young's modulus of 1.0 $\pm$ 0.1 TPa and strength of 130 GPa[3]. However, inclusion of grain boundaries reduces the Young's modulus to 600 GPa. The strength of polycrystalline graphene can also be 50% less than that of pristine monolayer graphene[6,12]. The results of nanoindentation test have shown that the failure behavior of graphene depends on the indentation site including grain center, grain boundaries, triple junctions and holes[13].

Reliable use of polycrystalline graphene sheet in industrial application necessitates fundamental understanding of the effect of grain size and grain boundaries orientation on the mechanical and fracture properties of graphene. The high resolution transmission electron microscopy images and molecular dynamics simulations indicate that grain boundaries (GBs) of graphene are composed of periodic and aperiodic sequences of pentagon–heptagon defects which act as dislocation cores.[14–18]. Graphene grain boundaries have distinct mechanical[19–21], chemical[20–22], electronic[20,23], and magnetic[20,24] properties that depends on their atomic arrangement.

Since grain boundaries act as the main defects in polycrystalline graphene sheets, it is necessary to include them in the models used for predicting fracture and failure properties of CVD graphene. Industries are interested in using large polycrystalline graphene sheets in the order of meter[25,26], however, due to the limitations associated with using atomic level simulations modeling fracture of large graphene sheets using molecular dynamics (MD) is not possible. Modeling the behavior of such large scale polycrystalline sheets requires other techniques such as finite element method[27] which can also incorporate the effect of grain boundaries[28,29].

One way to model crack initiation and growth using finite element method is to use cohesive zone models (CZM). By using CZM the stress singularity at the crack tip is removed by adding a cohesive zone of vanishing thickness ahead of the crack tip[30]. At the cohesive zone, the virtual cohesive surfaces are held together by a cohesive traction. The constitutive law of the cohesive zone is defined by prescribing a traction–separation law (TSL), also known as cohesive law, which defines the cohesive traction across the surfaces as a function of their separation distance. The crack growth occurs when the separation displacement of the cohesive surfaces at the physical crack tip reaches its critical value which corresponds to a zero traction across the surfaces.

Intergranular fracture using finite elements can be modeled by

[a] Department of Mechanical Engineering and Engineering Science, The University of North Carolina at Charlotte, Charlotte, NC 28223, USA. E-mail: atabarra@uncc.edu

† Electronic Supplementary Information (ESI) available: [details of any supplementary information available should be included here]. See DOI: 00.0000/00000000.

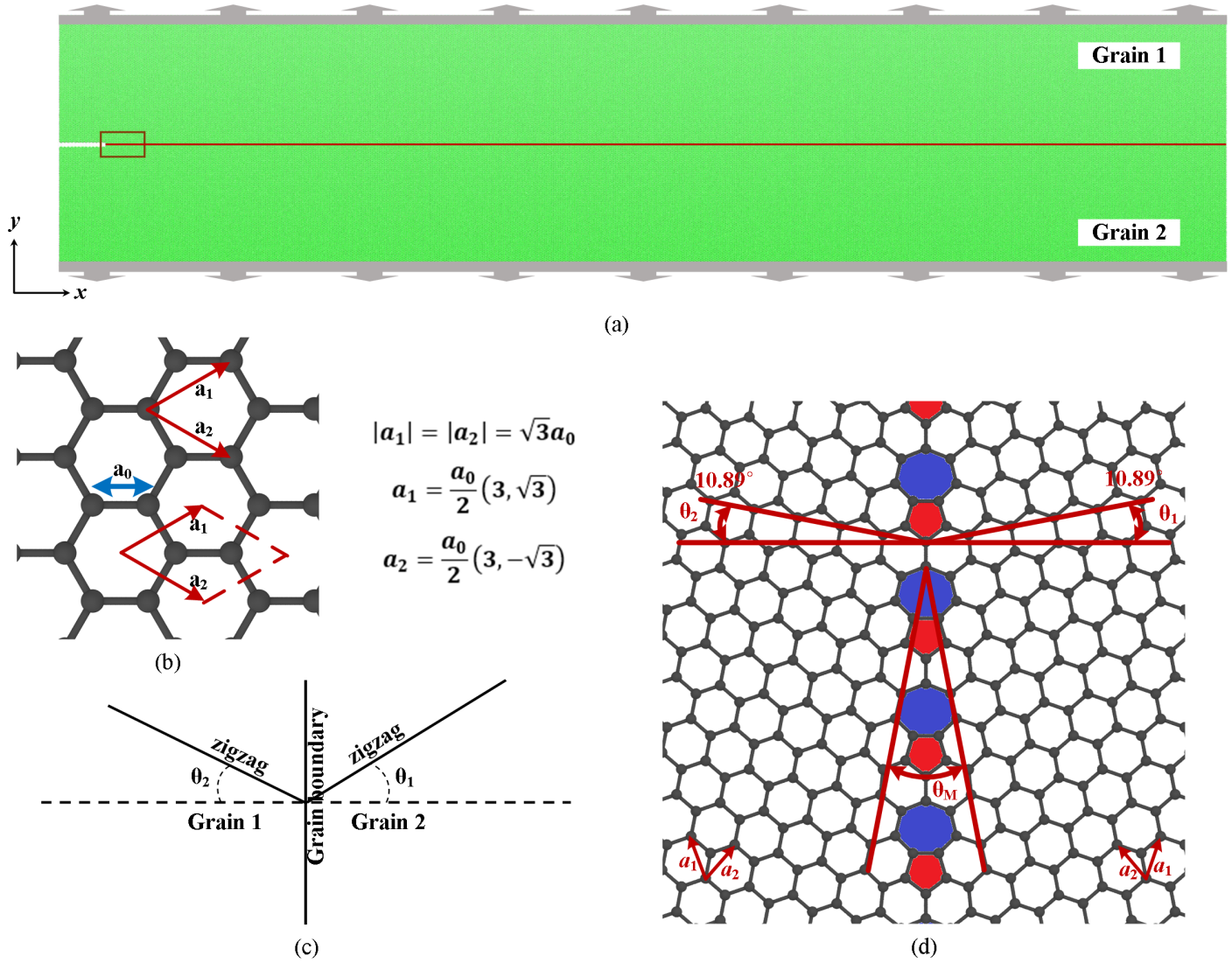

Fig. 1 (a) Schematic of the bicrystalline graphene panel with a grain boundary along the x–direction. The bicrystalline sheet has an initial crack along the grain boundary.(b) Hexagonal lattice structure of graphene. The unit cell is defined by the two basis vector a_1 and a_2 (red arrow) and contains two carbon atoms. (c) Grains tilt angle θ_1 and θ_2. (d) Representation of the misorientation angle θ_M of the grain boundary (GB).

incorporating cohesive elements along the GBs. The first requirement in using cohesive zone models for modeling failure is the availability of traction–separation laws (TSLs) which can accurately relates traction across the cohesive surfaces to their separations.

Extracting the cohesive laws using experimental work is challenging. In this paper, we use molecular dynamics method to extract the TSL of symmetric grain boundaries of graphene. In the last decade, atomistic simulations have dominated the studies on the mechanical and fracture properties of nanomaterials[31–43]. Molecular dynamic simulations that narrate the collective behavior of hundreds of thousands of atoms are a powerful tool to construct TSLs for graphene grain boundaries. Gall et al.[44] and Spearot et al.[45] have used MD simulations to scrutinize the cohesive forces at the interface of bi-materials. Yamakov et al.[46] proposed a methodology for using MD simulations to extract the TSLs of aluminum sheets with preexisting crack along the GB subjected to mode-I loading. A similar methodology was used by Zhou et al.[47] to extract the cohesive law for mixed mode loading conditions. Guin et al.[48] used this methodology with a double cantilever beams under mode-I loading to extract the TSLs of bicrystalline graphene. These studies considered only one or two grain boundaries. To be able to use cohesive laws in modeling behavior of polycrystalline graphene it is necessary to understand the TSLs of different grain boundaries with different atomic structure.

In this paper, we use molecular dynamics simulations to extract the TSLs of graphene grain boundaries using the methodology proposed by Yamakov et al.[46].Molecular dynamics simulations are conducted on bicrystalline graphene sheets as shown in Fig. 1(a). The TSLs are used to extract the work of separation or fracture energy of grain boundaries. We also investigate the

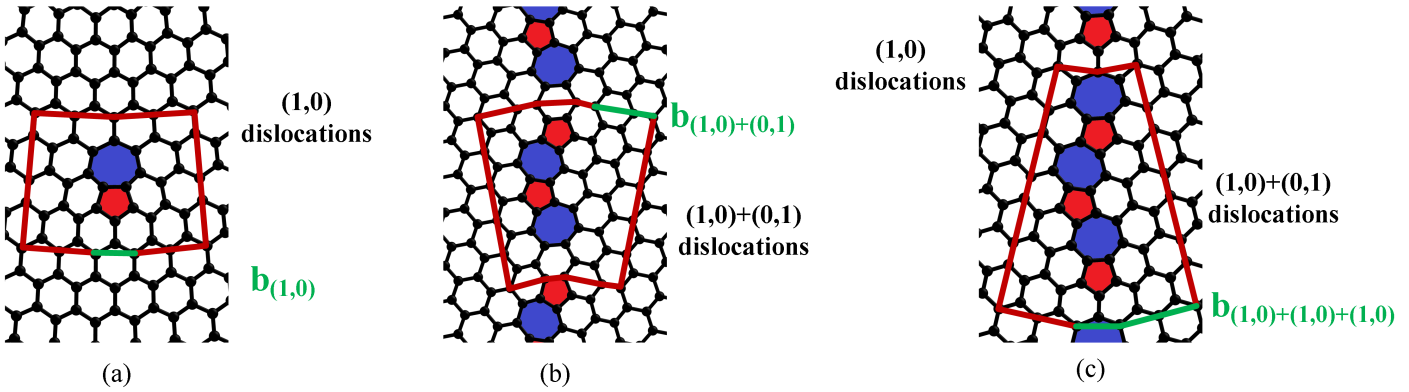

Fig. 2 Dislocation structures. (a) $(1,0)$ dislocations, (b) $(1,0)+(0,1)$ dislocations, and (c) $(1,0)$ and $(1,0)+(0,1)$ dislocations (modified (1,0)+(1,0)+(1,0) dislocations). The Burgers vector of each dislocation is shown in green.

traction-separation laws at different temperature to understand the effect of temperature on the work of separation at different misorientation angles.

2 Atomic structure of grain boundary (GB) and bicrystalline graphene

Graphene has a honeycomb lattice structure of sp^2 hybridized carbon atoms. The carbon-carbon bond length of graphene is $a_0 \approx 0.142$ nm which is the average bond distance of single and double covalent carbon-carbon bond. Its unit cell with lattice vectors $a_1 = \frac{a}{2}(3,\sqrt{3})$ and $a_2 = \frac{a}{2}(3,-\sqrt{3})$ consists of two carbon atoms as shown in Fig. 1(b).

The grain boundaries of graphene can be identified using two angles θ_1 and θ_2. These two angles define the angle between the normal vector of grain boundary with the zigzag direction in each grain, as shown in Fig. 1(c)–(d). The misorientation angle $\theta_M = \theta_1 + \theta_2$ represents the mutual orientation of the two pristine grains with respect to each other. Due to the six-fold rotational symmetry of graphene lattice $0^\circ \leq \theta_1, \theta_2 < \pi/3$ and $\theta_M \in (0^\circ, 60^\circ)$. Another parameter, $\theta_L = |\theta_1 - \theta_2|$, $[\theta_L \in (0^\circ, \theta_M)]$ describes the inclination of the grain boundary line with respect to symmetric configuration ($\theta_L = 0^\circ$). Due to the presence of two high symmetry directions in graphene, i.e. armchair and zigzag directions, the misorientation angles close to 0° and 60° are considered as low–angle grain boundaries along these directions, respectively.

Grain boundaries in graphene consists of an array of dislocations, each of which is represented by pentagon–heptagon pairs. In this paper, we study the fracture properties of symmetric grain boundaries with $\theta_1 = \theta_2$. Symmetric grain boundaries of graphene can be constructed by aligning $(1,0)$ dislocations along the grain boundary line. This leads to a discrete set of misorientation angles given by

$$\theta_M = 2\sin^{-1}\frac{|\mathbf{b}_{(1,0)}|}{2d_{(1,0)}} \tag{1}$$

where $\mathbf{b}_{(1,0)}$ is the Burgers vector of the dislocation as shown in Fig. 2(a) and $d_{(1,0)}$ is the distance between the dislocation cores. As the misorientation angle of grain boundary increase, the distance between the dislocations reduces as shown in Fig. 3(a)–(g). The closest pack between the dislocations lead to a misorientation angle of 21.79° where the dislocations are separated from each other by only a hexagon ring.

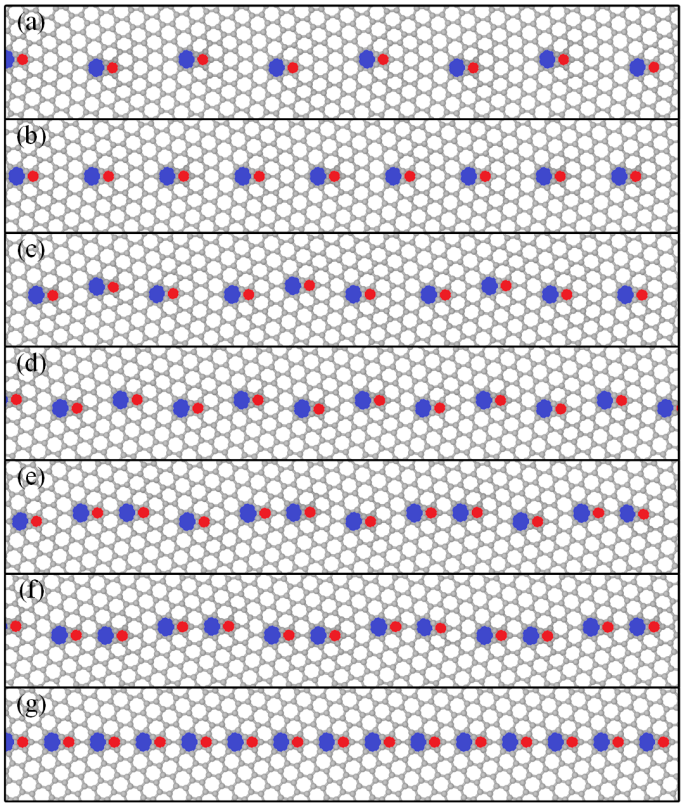

Fig. 3 The graphene GBs composed of $(1,0)$ dislocations. $(1,0)$ dislocations for different θ_M: (a) 10.99°, (b) 13.17°, (c) 15.18°, (d) 16.43°, (e) 17.99°, (f) 18.73°, and (g) 21.79°.

Dislocation pairs of $(1,0)+(0,1)$, shown in Fig. 2(b), can also be used to construct grain boundaries with misorientation angles between 32.20° and 60° [49]. The grain boundaries constructed using pairs of $(1,0)$ and $(0,1)$ dislocations are shown in Fig. 4(a)–(g). Similar to the previous case, when the misorientation an-

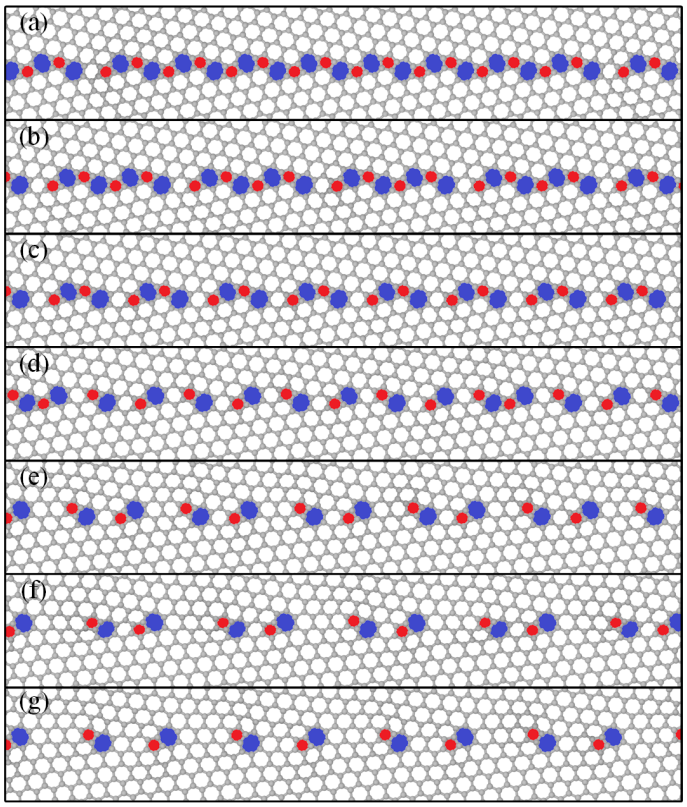

Fig. 4 Graphene grain boundaries composed of $(1,0)+(0,1)$ dislocations. (a) 33.13°, (b) 35.57°, (c) 38.12°, (d) 41.44°, (e) 44.88°, (f) 46.83°, and (g) 48.37°.

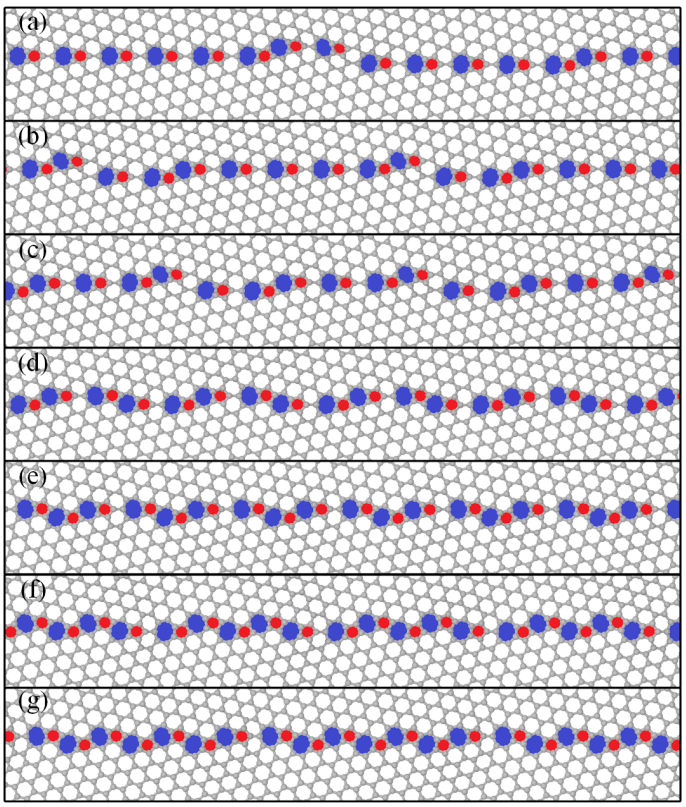

Fig. 5 Graphene grain boundaries composed of $(1,0)$ and $(1,0)+(0,1)$ dislocations. (a) 22.77°, (b) 23.71°, (c) 24.443°, (d) 26.01°, (e) 27.80°, (f) 29.41°, and (g) 30.17°.

gle between the two grain boundaries increases (θ_M approaching 32.20°), the distance between the dislocation pairs reduces until no spacing is available between dislocations at $\theta_M = 32.20°$.

To construct grain boundaries with misorientation angles between 21.79° and 32.20°, a combination of $(1,0)$ and $(1,0)+(0,1)$ dislocations can be used[49]. The grain boundaries constructed in this transition zone are shown in Fig. 5(a)–(g).

The grain boundaries shown in Fig. 3–Fig. 5 are constructed using the Voroni based algorithm proposed by Shekhawat et al.[17,18,50]. In this approach, first the triangular lattice dual to the graphene lattice of each grain is generated and the Voronoi diagram associated with each triangular lattice is constructed. This generates the honeycomb structure of graphene away from the grain boundary. To obtain pentagon–heptagon pairs along the grain boundary, Lioyd's algorithm[17,51] is employed to construct the centoridal Voronoi tessellation (CVT) associated with the triangular points close to the grain boundary while the location of the triangular lattice points away from the grain boundary are kept fixed. Finally, the conjugate gradient method is used to minimize the energy of the system which fine tunes the positions of the atoms.

3 Cohesive zone model

Cohesive zone models (CZM) are widely used in finite element modeling to describe local fracture processes[52,53]. The concept of cohesive zone model was first introduced by Barenblatt[54] and Dugdale[55] by using the traction on zones near the crack tip to model cohesive forces. Cohesive zone models are comprised of a region with vanishing thickness ahead of the physical crack tip including two cohesive surface subjected to cohesive traction as shown in Fig. 6(a). The displacement across the cohesive zone is discontinuous and the traction acting on the cohesive surfaces is a function of the displacement jump across the cohesive zones. The cohesive traction acting on the cohesive surfaces can be described as a function of the separation between the surfaces by a traction–separation law also known as cohesive law. A typical TSL is shown in Fig. 6(b). The relation between the traction and separation of a cohesive zone can be written as

$$t = t_m f\left(\frac{\delta}{\delta_c}\right), \tag{2}$$

where t_m is the maximum cohesive traction, δ_c is the critical separation, and f is a dimensionless function that describe the shape of the traction–separation curve. The maximum cohesive traction t_m is the cohesive strength and occurs at δ_m which represents the separation distance where the irreversible failure process initiates[48]. The critical displacement δ_c represents the separation distance where no cohesive traction exists between the two surfaces. The cohesive energy density S_e represents the work of separation

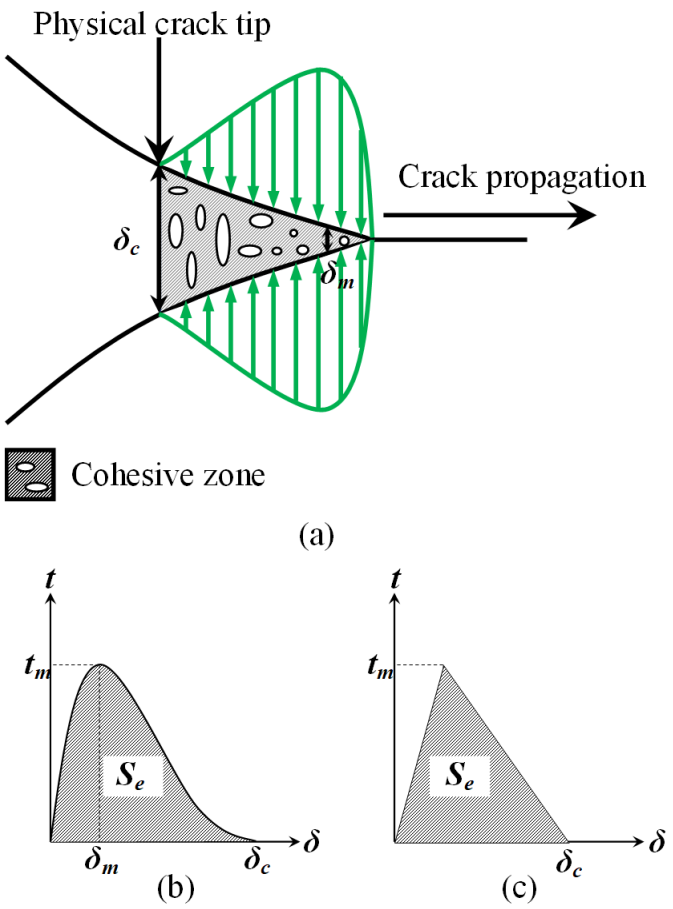

Fig. 6 (a) Schematic view of cohesive zone ahead of crack where cohesive traction t associated with the to the crack openings δ. (b) Characteristic profile of a TSL in the CZM. (c) Typical bilinear TSL.

per unit area of cohesive surfaces and is obtained by

$$S_e = \int_0^{\delta_c} t(\delta)\, d\delta \tag{3}$$

The work of separation per unit area of cohesive surfaces is the area under the traction-separation curve and correspond to the energy absorbed by the fracture process per unit crack surface growth. To be consistent with Griffith energetic approach, the fracture energy G_c should be equal to the work of separation per unit area of cohesive surfaces S_e.

Different forms of cohesive laws including bilinear, trapezoid, sinusoidal and exponential have been proposed and used to model crack initiation and growth[52–59]. As an example, the bilinear cohesive law which can mathematically be represented as

$$t = \begin{cases} \frac{t_m}{\delta_m}\delta & 0 \le \delta \le \delta_m \\ \frac{t_m}{\delta_c - \delta_m}(\delta_c - \delta) & \delta_m \le \delta \le \delta_c \\ 0 & \delta \ge \delta_c \end{cases} \tag{4}$$

is shown in Fig. 6(c). For this model, the separation energy can be obtained using

$$S_e = \frac{1}{2} t_m \delta_c. \tag{5}$$

4 Computational method

4.1 Description of molecular dynamics simulations

Molecular dynamics (MD) simulations are used to extract the TSLs of the grain boundaries shown in Figs. 3 to 5. MD simulations are conducted using the freely available Large-scale Atomic/Molecular Massively Parallel Simulator (LAMMPS)[60]. Second–generation empirical reactive bond–order (REBO2)[61] interatomic potential with an environment–dependent modified cutoff scheme (REBO2+S) of Pastewka et al.[62] is used to model the interaction between the carbon atoms. The REBO2+S potential can model the C–C bond-breaking events[62–64] and accurately predict the mechanical properties and fracture properties of graphene[21,65,66].

The bicrystalline graphene sheets used in this study have a width of 35 nm and length of 140 nm with grain boundaries in the x–direction. An initial crack of length 5 nm $\sim$ 5.5 nm is defined along the grain boundaries by removing a few layers of atoms. Two reflective walls are defined at a distance of 0.3 nm in the z–direction parallel to the panel to constrain the out–of–plane movement while the local motions of the atoms remain 3D. These constraints do not affect the quantitative observations of simulations or qualitative response of the fracture process of the bi-material interface.

The equations of motion are integrated using the velocity Verlet scheme employing an integration time step of 1 femtosecond. The initial configuration of the system are obtained by minimizing the potential energy of the system using the conjugate gradient method to remove any initial internal stress. After the minimization, the Berendsen thermostat is used in a micro canonical ensemble (NVE) for 50 ps to raise the system temperature to the desired temperature. Finally, to stabilize the system, the model is equilibrated in a canonical ensemble (NVT) for 50 ps at the temperature of 0.1 K.

After the equilibration stages, the model is subjected to tensile loading in an NVT ensemble by elongating the domain width in the y–direction at a strain rate of $2.5 \times 10^8\,\mathrm{s}^{-1}$ while the domain can relax in the lateral directions. Previous studies have shown that a strain rate less than $2 \times 10^9\,\mathrm{s}^{-1}$ has negligible impact on the fracture properties of graphene–like 2D materials[43], therefore the strain rate used in our simulations is not expected to significantly affect the results. During the elongation process, the y and z–component of the forces acting on a strip of atoms at the top and bottom edges of the panel are set to zero to prevent them from moving in these directions while they are free to move in the x–direction.

4.2 Extraction of the traction–separation laws

We follow the methodology proposed by Yamakov et al.[46] to extract the traction–separation laws (TSLs) of grain boundaries. In this technique, a strip of atoms in front of the crack tip along the crack propagation path is used to extract TSL. Since in this study

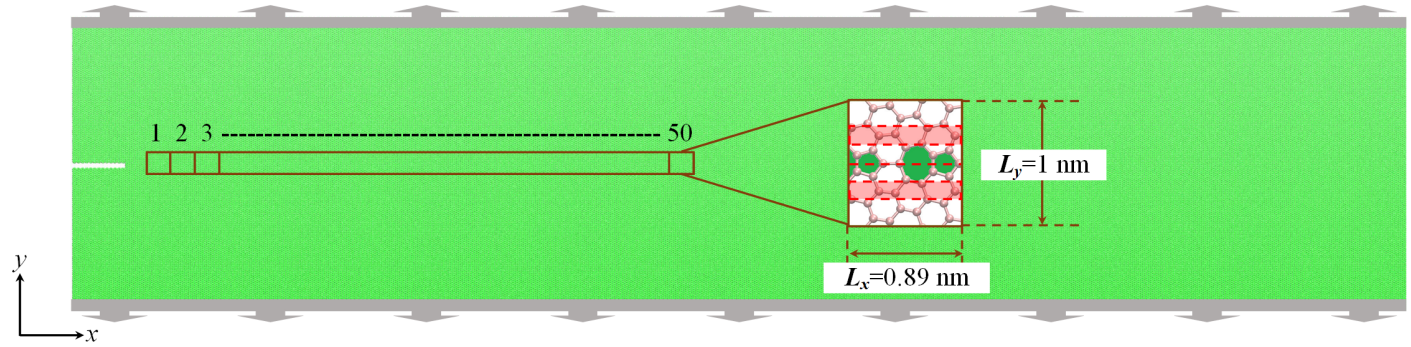

Fig. 7 Cohesive zone volume element (CZVE) used along the grain boundary at the vicinity of crack tip. The atoms shown in red are used to calculate the separation distance.

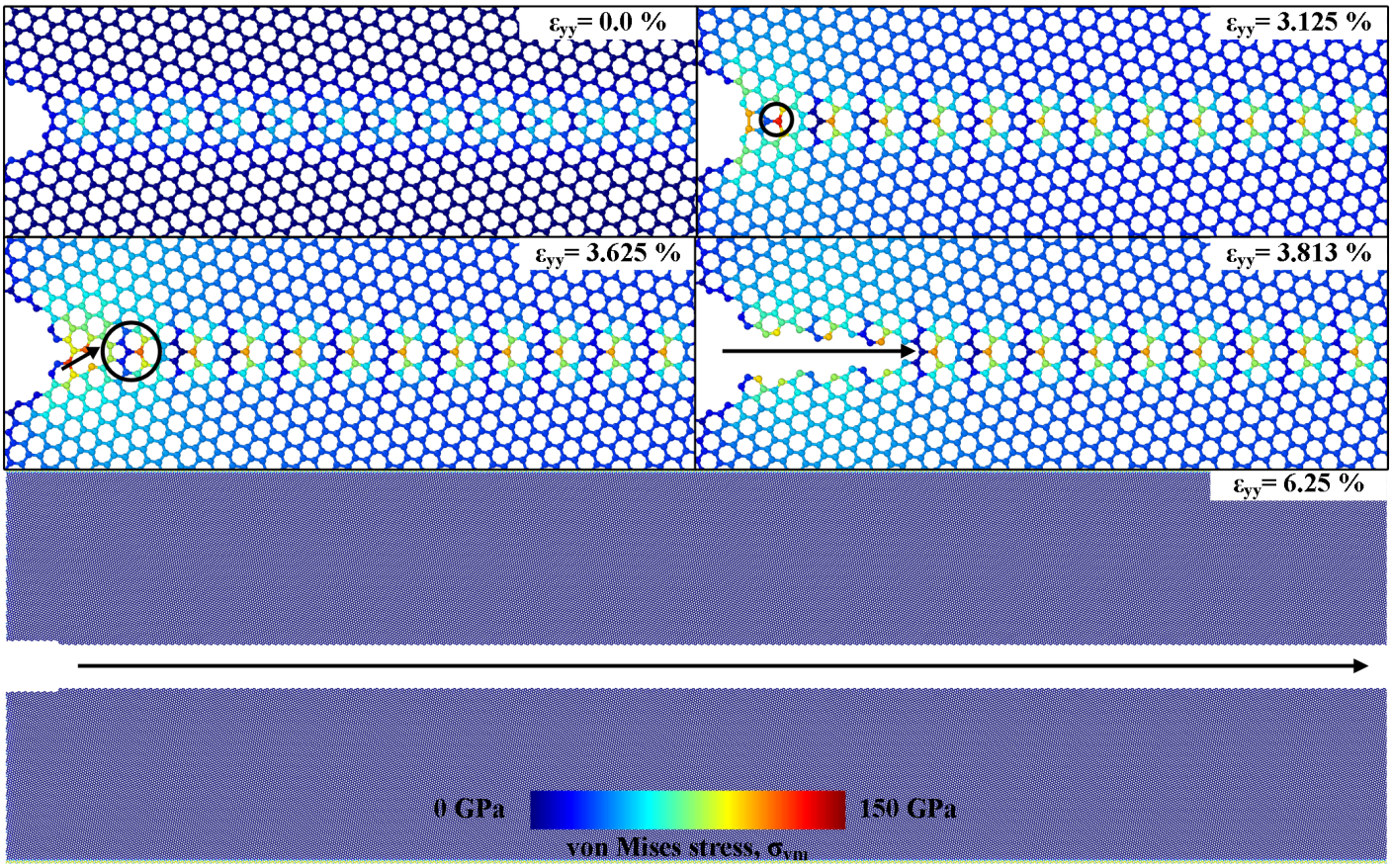

Fig. 8 The crack propagation mechanism along a GB with misorientation angle of $\theta_M = 21.79^\circ$ comprised of $(1,0)$ dislocations. The contour plots represent the von Mises stress of atomic stress.

the crack path is along the grain boundary, the strip of atoms is centered at the grain boundary line and has a height of L_y. The strip is divided into $N = 50$ cohesive zone volume elements (CZVE) with a width of L_x as shown in Fig. 7. The atoms located within a CZVE in the reference configuration are assigned to that CZVE.

The virial formulation[67] can be used to compute the stresses in the CZVE

$$\sigma_{ij}^{\alpha} = -\frac{1}{V^{\alpha}}\left[m^{\alpha} v_i^{\alpha} v_j^{\alpha} + \frac{1}{2}\sum_{\beta \in N^k} r_i^{\alpha\beta} f_i^{\alpha\beta}\right], \qquad (6)$$

where i and j define the axis of the coordinate system and take values of 1, 2, and 3, σ_{ij}^{α} is the stress of atom α, m_{α} is the mass of atom α, $\boldsymbol{v}^{\alpha}$ is the relative velocity of atom α with respect to macroscopic motion of the system, $\mathbf{r}^{\alpha\beta} = \mathbf{r}^{\alpha} - \mathbf{r}^{\beta}$ is the displace-

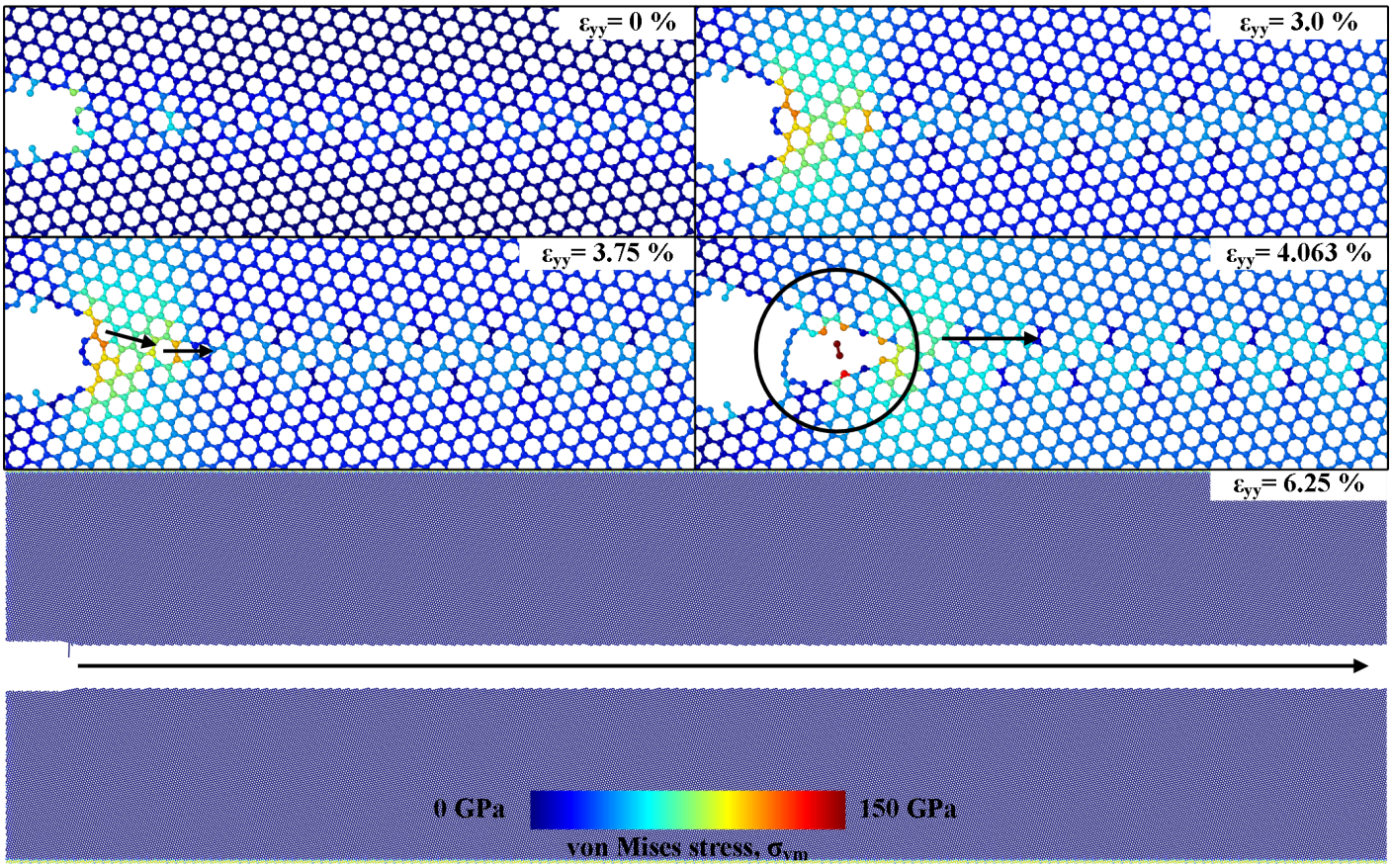

Fig. 9 The crack propagation mechanism along a GB with misorientation angle of $\theta_M = 33.13^\circ$ comprised of $(1,0)+(0,1)$ dislocations. The contour plots represent the von Mises stress of atomic stress.

ment vector between atoms α and β, $\mathbf{f}^{\alpha\beta}$ is the interatomic force between atom α and β, and V^α is the volume of atom α in the current configuration. The volume of atoms is approximated using their volume in the pristine honeycomb graphene lattice as

$$V_0^{hon} = \frac{3\sqrt{3}}{4} a^2 t \tag{7}$$

with $a \approx 0.142\,\text{nm}$ is the interatomic distance of C-C bond, and t is the thickness of graphene which is taken equal to $0.335\,\text{nm}$.

The virial stress is the microscopic definition of the Cauchy stress for discrete systems[68,69]. The virial stress obtained from the molecular dynamics simulation should be averaged over time in order for it to be equivalent to the continuum Cauchy stress. The Cauchy stress of the kth cohesive element is obtained by both time and space averaging of atomic virial stresses over the volume of the CZVE

$$\sigma_{ij}^k = \frac{1}{N_t V^k} \sum_{t=1}^{N_t} \sum_{\alpha \in A^k} V^\alpha \sigma_{ij}^\alpha(t), \tag{8}$$

where A^k is the set of atoms located within the kth CZVE, $N_t = 2500$ is the number of time steps t in the time interval of $2.5\,\text{ps}$ over which the time averaging is conducted, and V^k is the volume of the kth CZVE and computed as the number of atoms in the kth CZVE times the volume of carbon atom V_0^{hon}. The calculation of V^k neglects the effect of change in atom volumes dues to the tensile strain and inhomogeneities in the atoms volume introduced by the pentagon-heptagon defect as well as the high strains at the crack tip. The cohesive traction of each CZVE acting on the crack processing zone ahead of the crack tip is equal to the y–component of the Cauchy stress σ_{yy} calculated from Eq. (8).

The separation distance of the kth CZVE is calculated as the average distance between the centroids of the upper and lower portions of this CZVE. The separation distance $\delta = d - d_0$ where d and d_0 are the y–component of distance between the centroids of the upper and lower portion of the CZVEs in the initial and final configurations, respectively. Similar to traction, the distance d is calculated by time averaging over 0.25 ps using 2500 time steps.

In this paper, the cohesive zone volume elements (CZVE) have a length of $L_x = 0.89$ nm in the x–direction. The size of the cohesive zone elements is an important parameter which affects the accuracy of the results. The cohesive zone elements should be small enough to capture the high stress and strain gradients at the crack tip and large enough to ensure that averaging the virial stress over the CZVE is equivalent to the Cauchy stress. Using Hillerborg et al.[70] approach, the length of the cohesive zone in front of a crack tip in graphene is estimated to be 2.6 nm[48]. By choosing $L_x = 0.89$ nm, the cohesive zone is resolved by three cohesive elements which is enough to capture the stress and strain

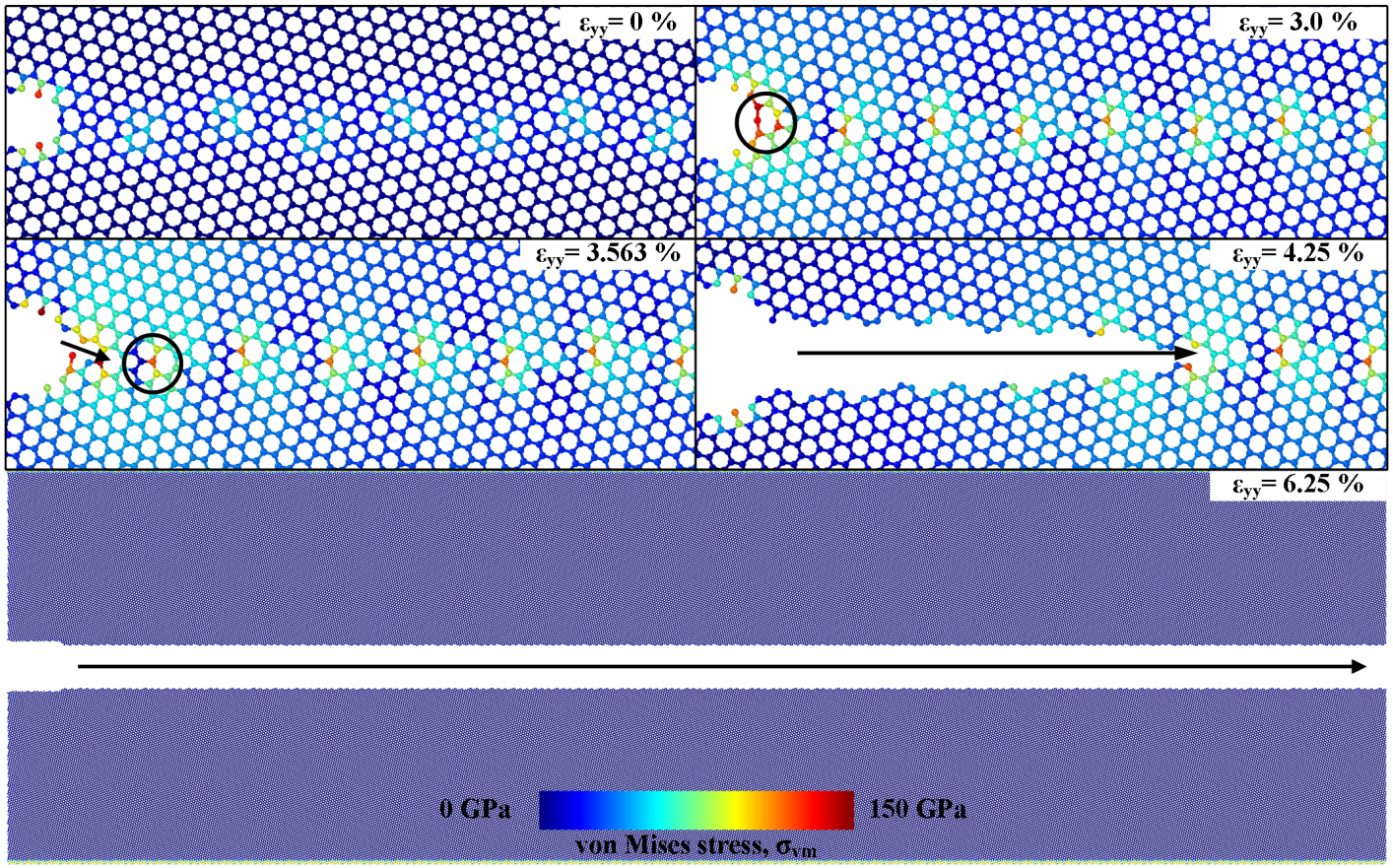

Fig. 10 The crack propagation mechanism along a GB with misorientation angle of $\theta_M = 26.01^\circ$ comprised of $(1,0)$ and $(1,0)+(0,1)$ dislocations. The contour plots represent the von Mises stress of atomic stress.

gradient ahead of the crack tip. The length of the cohesive zone affect the value of maximum traction t_m but does not impact the value of separation energy S_e. Since t_m represents the strength of the grain boundary before a crack initiates, the value of L_x should be chosen such that t_m matches with the grain boundary strength before defect. Choosing $L_x = 0.89$ nm satisfies this condition as well[21,48,71]. The size of the cohesive elements in the y–direction is $\delta_y = 1$ nm. This size is chosen large enough to encompass the prestressed fields generated by the grain boundary heptagon–pentagon defects.

5 Results and discussion

We have used the methodology described in the previous section to extract the traction–separation laws (TSLs) of high angle symmetric grain boundaries with misorientation angle (θ_M) between $10.99^\circ \sim 48.37^\circ$ as shown in Figs. 3 to 5. For such grain boundaries, the crack propagation path remains along the grain boundary. For low angle grain boundaries with θ_M near 0° and 60°, the crack does not grow along the grain boundary and kinks to propagates along a zigzag direction in one of the grains. This deviation in the crack path is due to the large separation of the heptagon–pentagon defects with several hexagonal rings between these defects. When the crack reaches the hexagonal rings it kinks to grow along a zigzag path.

5.1 Crack propagation

The propagation path of cracks along the grain boundaries at different tensile strain loading are shown in Figs. 8 to 10. The crack propagation mechanism along the grain boundary with misorientation angle $\theta_M = 21.79^\circ$ which is composed only of $(1,0)$ dislocations is shown in Fig. 8. As shown in Fig. 8, by increase in the tensile strain, first the bond at the crack tip breaks. By further increase in the strain, the C–C bond of the first heptagon ring ahead of the crack tip breaks. This process is followed by the failure of the bond connecting the pentagon–heptagon pairs and the C–C bond of the next heptagon ring. This process repeats itself until crack reaches the end of the panel.

Our MD results show that the crack growth along other grain boundaries comprised of $(1,0)$ dislocation follows a similar bond breaking mechanism. For lower angle grain boundaries studied in this paper, the crack growth was associated with the creation of nanovoids between the pentagon–heptagon pairs ahead of the crack tip as shown in Fig. 8.

The crack growth along the grain boundaries composed of only $(1,0)+(0,1)$ dislocations, or both $(1,0)$ and $(1,0)+(0,1)$ dislocations are shown in Figs. 9 and 10. The crack growth along these grain boundaries is associated with the failure of an interface bond between the pentagon and heptagon defect. This bond failure is not usually occurs at the crack tip and its failure leads

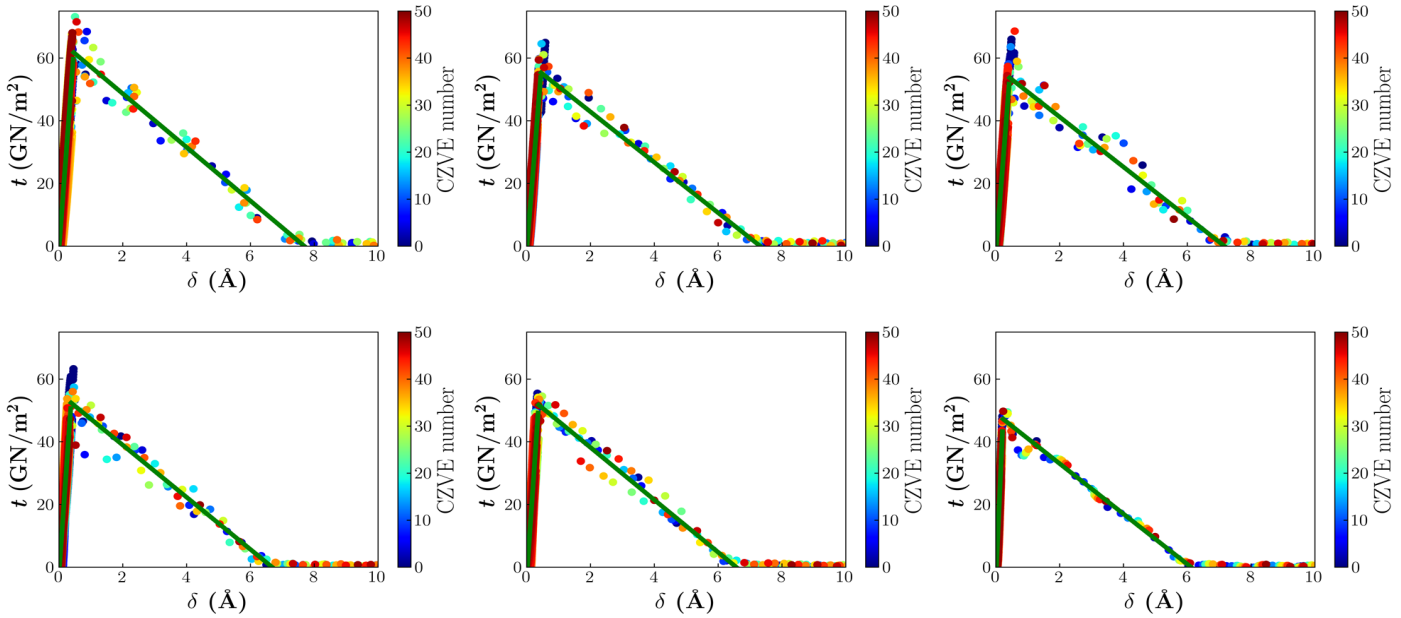

Fig. 11 The traction–separation points obtained from the 50 CZVEs ahead of the crack tip along the grain boundaries composed of $(1,0)$ dislocations. A bilinear curve is fitted to the points.

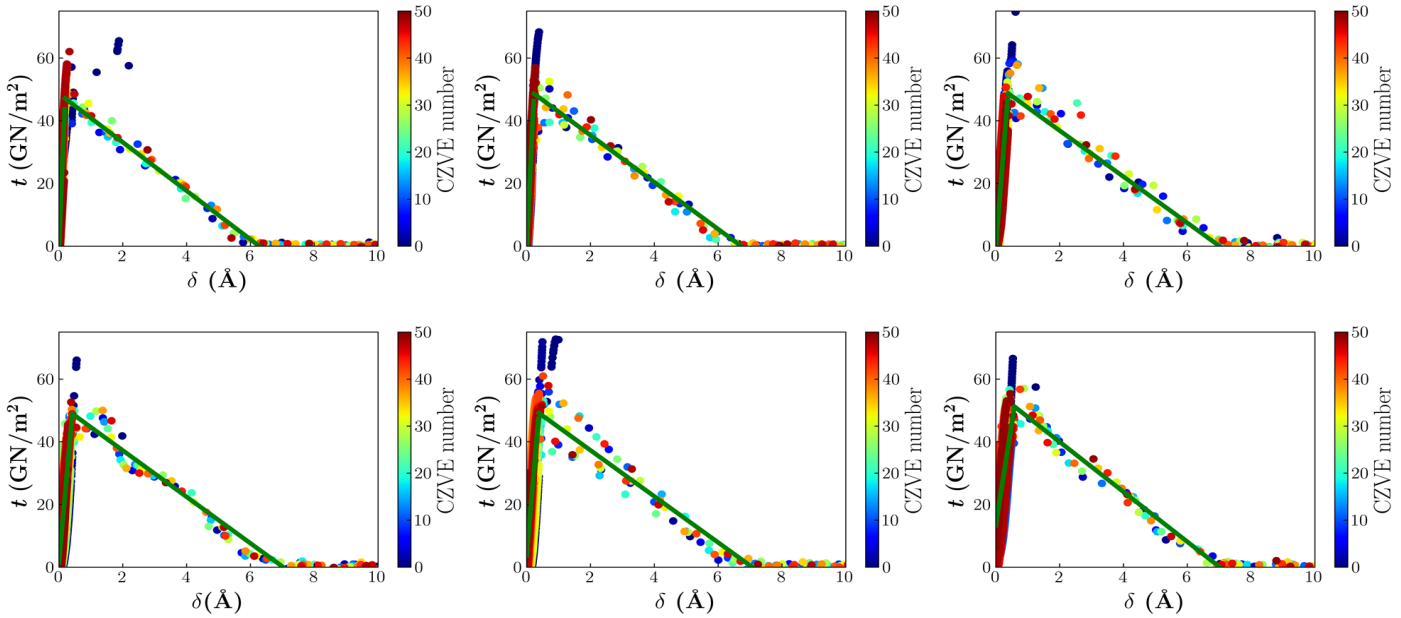

Fig. 12 The traction–separation points obtained from the 50 CZVEs ahead of the crack tip along the grain boundaries composed of $(1,0)+(0,1)$ dislocations. A bilinear curve is fitted to the points.

to the generation of nanovoids along the crack path. Further increase in the tensile strain leads to the failure of bonds at the crack tip which leads to the coalescence of the nanovoids and the pre–existing crack and results in the crack growth.

5.2 Traction-separation law

The traction and separation values of all the CZVEs ahead of the crack tip at different strain levels at a temperature of 0.1 K are calculated and plotted in Figs. 11 to 13. It can be seen that the traction separation law of all the grain boundaries have a bilinear from; with increase in the separation displacement the cohesive traction increases until reaching the maximum traction point t_m after that it decrease linearly unit it reaches a zero stress at the critical separation δ_c. The traction–separation data points are fitted using two lines, one before the maximum traction and the other after it as shown in the Figs. 11 to 13. The intersection

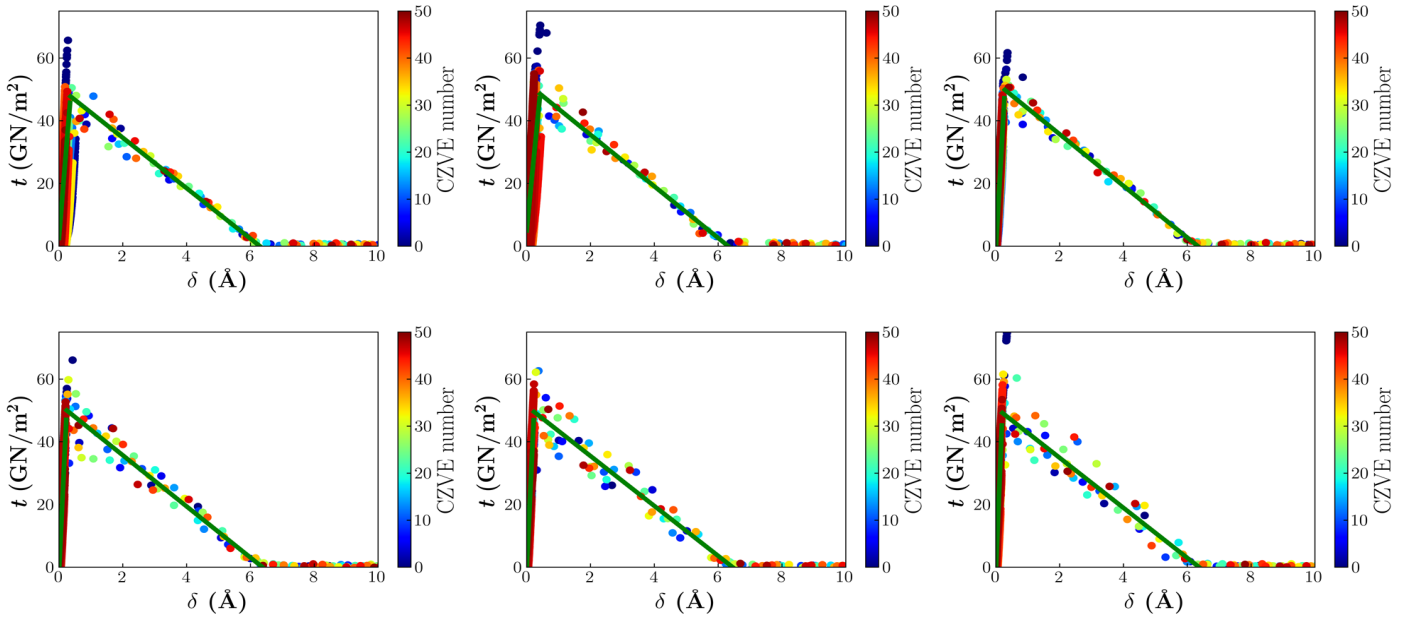

Fig. 13 The traction–separation points obtained from the 50 CZVEs ahead of the crack tip along the grain boundaries composed of $(1,0)$ and $(1,0)+(0,1)$ dislocations. A bilinear curve is fitted to the points.

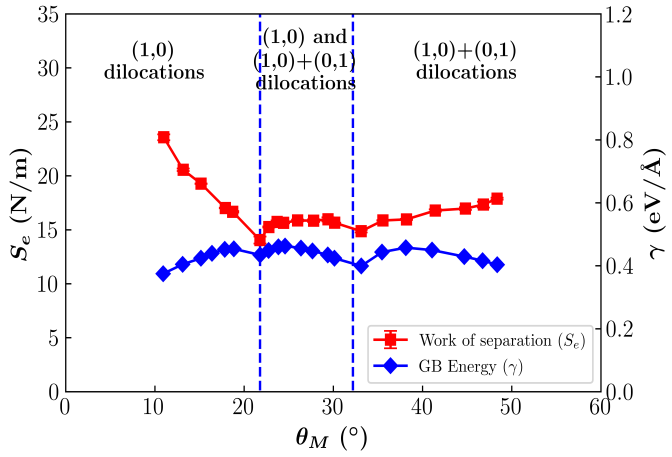

Fig. 14 Work of separation (S_e) and grain boundary energy (γ)[49] versus grain boundary misorientation angle.

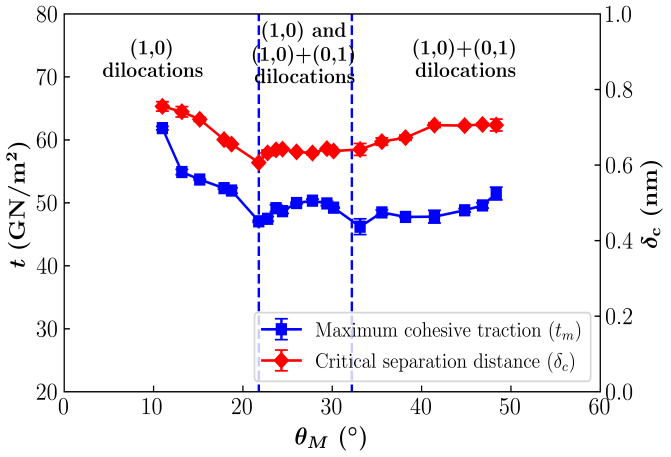

Fig. 15 Maximum cohesive traction and critical separation distance versus grain boundary misorientaion angle.

point of the two fitted lines is considered as the maximum cohesive traction t_m which does no necessarily match with the data point with the highest value of traction.

The work of separations calculated from the TSLs are plotted as a function of grain boundaries misorientation angles in Fig. 14. For the purpose of comparison the grain boundary energies[49] are plotted in the same graph. It can be seen that for low angle grain boundaries the trend of the work of separation is reverse of that of grain boundary energy; by increase in the grain boundary energy the work of separation decreases. Such a relationship does not exist between the work of separation and grain boundary energy for high angle grain boundaries.

For the grain boundaries comprised of only $(1,0)$ dislocations, increasing the grain boundary misorientation angle leads to a reduction in the separation energy. On the other hand, for grain boundaries comprised of $(1,0)+(0,1)$ dislocations, as the misorientation angle approaches 60◦ the dislocation density decreases. Hence for this types of grain boundaries, the work of separation increases as the misorientation angle approaches 60°. Finally, in the transition zone where the grain boundaries are comprised of $(1,0)$ and $(1,0)+(0,1)$, the separation energy does not change significantly as the misorientation angle increases.

The maximum cohesive traction which represents the strength of grain boundary and the critical separation distance of grain boundaries are shown in Fig. 15. For the grain boundaries comprised of $(1,0)$ or $(1,0)+(0,1)$ dislocations, as a general trend, by

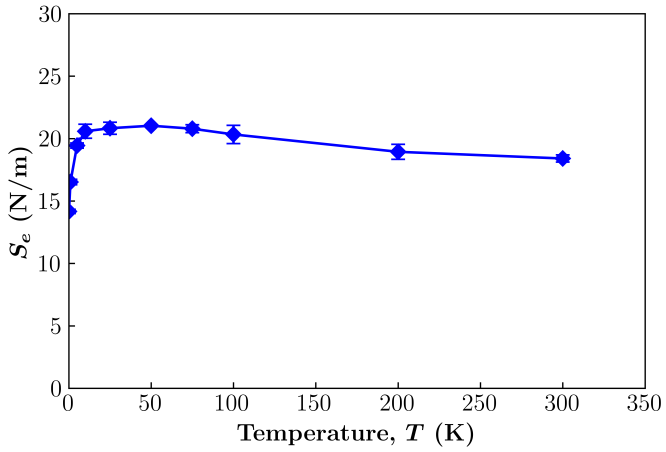

Fig. 16 Effect of temperature on the work of separation on the bicrystalline graphene with $\theta_M = 21.79°$.

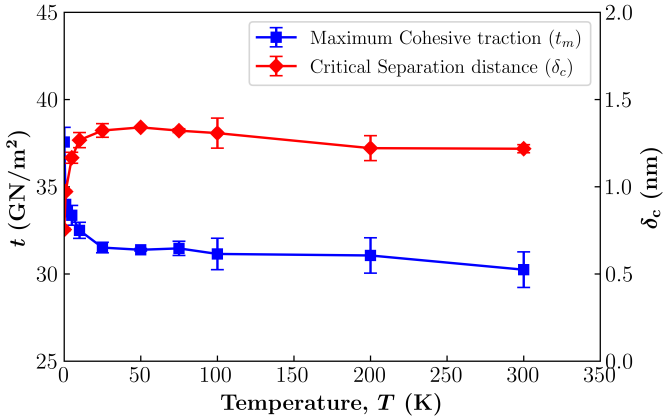

Fig. 17 Effect of temperature on the maximum cohesive traction and critical separation distance on the bicrystalline graphene with $\theta_M = 21.79°$.

increase in the grain boundaries misorientation angle the grain boundaries strength reduce and they fail at smaller separation distances which leads to a lower work of separation for such grain boundaries. For the grain boundaries composed of $(1,0)$ and $(1,0)+(0,1)$ dislocations, the separation distance does not change as the misorientation angle increases. For these grain boundaries, the maximum cohesive traction first increases slightly and then decreases.

5.3 Impact of temperature on the separation energy

The impact of temperature on the work of separation (S_e) of GBs is studied by obtaining the TSL at various temperatures in the range of 0.1 K to 300 K. The separation energy of the grain boundary with misorientation angle of $\theta_M = 21.79°$ as a function of temperature is shown in Fig. 16. This graph indicates that with an increase in the temperature, the separation energy increases quickly from 14 N/m at 0.1 K to 21 N/m at 25 K. The separation energy remains constant from 20 K to 50 K and then reduces to 18 N/m at the room temperature of 300 K.

The maximum cohesive traction t_m and the critical separation distance δ_c are plotted in Fig. 17. And it observed that the trend of change of the maximum cohesive traction versus temperature is opposite of that for the critical separation distance. Similar relations between maximum cohesive traction and critical separation distance versus temperature has been observed for hydrogeneted grain boundary of graphene[21]. The higher critical separation distance at higher temperature indicates that the fracture at higher temperature is more ductile.

6 Conclusion

In this present study, MD simulations were used to study the fracture properties of symmetric grain boundaries in graphene. A bicrystalline graphene sheet with an existing crack were used to extract the TSLs of the grain boundaries. The TSLs obtained from the MD simulations have a bilinear form for all bicrystalline graphene. The results indicated that the grain boundary with high dislocations density have a smaller separation energy. The impact of temperature on the work of separation of grain boundaries are studied. The result showed that by increasing in the temperature from 0.1 K to 300 K first the separation energy increases and then reduces slightly.

Conflicts of interest

The authors report no conflict of interest.

Acknowledgements

The authors are grateful for the research support of the National Science Foundation through grant CMMI-1563224 to the University of North Carolina at Charlotte (UNCC). All the simulations were performed on the University Research Computing (URC) High Performance Computing (HPC) clusters at the University of North Carolina at Charlotte.

Notes and references

1 A. Geim and K. Novoselov, *Nature Materials*, 2007, **6**, 183–191.
2 A. A. Balandin, S. Ghosh, W. Bao, I. Calizo, D. Teweldebrhan, F. Miao and C. N. Lau, *Nano letters*, 2008, **8**, 902–907.
3 C. Lee, X. Wei, J. W. Kysar and J. Hone, *science*, 2008, **321**, 385–388.
4 M. I. Katsnelson, *Materials today*, 2007, **10**, 20–27.
5 A. K. Geim, *science*, 2009, **324**, 1530–1534.
6 B. Liu and K. Zhou, *Progress in Materials Science*, 2019, **100**, 99–169.
7 K. S. Novoselov, A. K. Geim, S. V. Morozov, D. Jiang, Y. Zhang, S. V. Dubonos, I. V. Grigorieva and A. A. Firsov, *science*, 2004, **306**, 666–669.
8 G. Eda, G. Fanchini and M. Chhowalla, *Nature nanotechnology*, 2008, **3**, 270–274.
9 C. Berger, Z. Song, T. Li, X. Li, A. Y. Ogbazghi, R. Feng, Z. Dai, A. N. Marchenkov, E. H. Conrad, P. N. First *et al.*, *The Journal of Physical Chemistry B*, 2004, **108**, 19912–19916.
10 X. Li, W. Cai, J. An, S. Kim, J. Nah, D. Yang, R. Piner, A. Ve-

lamakanni, I. Jung, E. Tutuc *et al.*, *science*, 2009, **324**, 1312–1314.
11 A. Reina, X. Jia, J. Ho, D. Nezich, H. Son, V. Bulovic, M. S. Dresselhaus and J. Kong, *Nano letters*, 2009, **9**, 30–35.
12 J. Kotakoski and J. C. Meyer, *Physical Review B*, 2012, **85**, 195447.
13 Z. Sha, Q. Wan, Q. Pei, S. Quek, Z. Liu, Y. Zhang and V. Shenoy, *Scientific reports*, 2014, **4**, 1–6.
14 P. Y. Huang, C. S. Ruiz-Vargas, A. M. Van Der Zande, W. S. Whitney, M. P. Levendorf, J. W. Kevek, S. Garg, J. S. Alden, C. J. Hustedt, Y. Zhu *et al.*, *Nature*, 2011, **469**, 389–392.
15 K. Kim, Z. Lee, W. Regan, C. Kisielowski, M. Crommie and A. Zettl, *ACS nano*, 2011, **5**, 2142–2146.
16 H. I. Rasool, C. Ophus, Z. Zhang, M. F. Crommie, B. I. Yakobson and A. Zettl, *Nano letters*, 2014, **14**, 7057–7063.
17 C. Ophus, A. Shekhawat, H. Rasool and A. Zettl, *Physical Review B*, 2015, **92**, 205402.
18 A. Shekhawat and R. O. Ritchie, *Nature communications*, 2016, **7**, 1–8.
19 F. Banhart, J. Kotakoski and A. V. Krasheninnikov, *ACS nano*, 2011, **5**, 26–41.
20 L. Liu, M. Qing, Y. Wang and S. Chen, *Journal of Materials Science & Technology*, 2015, **31**, 599–606.
21 M. S. Elapolu and A. Tabarraei, *The Journal of Physical Chemistry C*, 2020, **124**, 17308–17319.
22 D. Boukhvalov and M. Katsnelson, *Nano letters*, 2008, **8**, 4373–4379.
23 G. M. Rutter, J. Crain, N. Guisinger, T. Li, P. First and J. Stroscio, *Science*, 2007, **317**, 219–222.
24 M. Akhukov, A. Fasolino, Y. Gornostyrev and M. Katsnelson, *Physical Review B*, 2012, **85**, 115407.
25 Y. Zhu, H. Ji, H.-M. Cheng and R. S. Ruoff, *National Science Review*, 2018, **5**, 90–101.
26 D.-Y. Wang, I.-S. Huang, P.-H. Ho, S.-S. Li, Y.-C. Yeh, D.-W. Wang, W.-L. Chen, Y.-Y. Lee, Y.-M. Chang, C.-C. Chen *et al.*, *Advanced materials*, 2013, **25**, 4521–4526.
27 T. J. Hughes, *The finite element method: linear static and dynamic finite element analysis*, Courier Corporation, 2012.
28 A. K. Kanjarla, P. Van Houtte and L. Delannay, *International Journal of Plasticity*, 2010, **26**, 1220–1233.
29 H. Lim, M. Lee, J. Kim, B. Adams and R. Wagoner, *International Journal of Plasticity*, 2011, **27**, 1328–1354.
30 T. L. Anderson and T. Anderson, *Fracture Mechanics: Fundamentals and Applications*, CRC Press, 2005.
31 P. Zhang, L. Ma, F. Fan, Z. Zeng, C. Peng, P. E. Loya, Z. Liu, Y. Gong, J. Zhang, X. Zhang *et al.*, *Nature communications*, 2014, **5**, 3782.
32 H. Yin, H. J. Qi, F. Fan, T. Zhu, B. Wang and Y. Wei, *Nano letters*, 2015, **15**, 1918–1924.
33 A. Tabarraei and X. Wang, *Materials Science and Engineering: A*, 2015, **641**, 225–230.
34 M. S. Elapolu, A. Tabarraei, X. Wang and D. E. Spearot, *Engineering Fracture Mechanics*, 2019, **212**, 1–12.
35 N. Liu, J. Hong, R. Pidaparti and X. Wang, *Nanoscale*, 2016, **8**, 5728–5736.
36 A. Tabarraei and X. Wang, *Applied Physics Letters*, 2016, **108**, 181904.
37 A. Tabarraei, S. Shadalou and J.-H. Song, *Computational Materials Science*, 2015, **96**, 10–19.
38 H. Bao, Y. Huang, Z. Yang, Y. Sun, Y. Bai, Y. Miao, P. K. Chu, K. Xu and F. Ma, *The Journal of Physical Chemistry C*, 2018, **122**, 1351–1360.
39 M. I. R. Shishir and A. Tabarraei, ASME International Mechanical Engineering Congress and Exposition, 2019, p. V009T11A051.
40 R. M. Muthoka, M. I. R. Shishir, H. C. Kim, J. W. Kim and J. Kim, Nano-, Bio-, Info-Tech Sensors, and 3D Systems II, 2018, p. 105971F.
41 A. I. Shiave, R. P. S. Tomar, I. P. Espinosa and R. Mohan, *Advanced Science, Engineering and Medicine*, 2019, **11**, 1187–1201.
42 M. I. R. Shishir and A. Tabarraei, ASME International Mechanical Engineering Congress and Exposition, 2020, p. V012T12A035.
43 M. I. R. Shishir, M. S. Elapolu and A. Tabarraei, *Mechanics of Materials*, (in press).
44 K. Gall, M. Horstemeyer, M. Van Schilfgaarde and M. Baskes, *Journal of the Mechanics and Physics of Solids*, 2000, **48**, 2183–2212.
45 D. E. Spearot, K. I. Jacob and D. L. McDowell, *Mechanics of Materials*, 2004, **36**, 825–847.
46 V. Yamakov, E. Saether, D. R. Phillips and E. H. Glaessgen, *Journal of the Mechanics and Physics of Solids*, 2006, **54**, 1899–1928.
47 X. Zhou, J. Zimmerman, E. Reedy Jr and N. Moody, *Mechanics of Materials*, 2008, **40**, 832–845.
48 L. Guin, J. L. Raphanel and J. W. Kysar, *Journal of Applied Physics*, 2016, **119**, 245107.
49 T.-H. Liu, G. Gajewski, C.-W. Pao and C.-C. Chang, *Carbon*, 2011, **49**, 2306–2317.
50 A. Shekhawat, C. Ophus and R. O. Ritchie, *RSC advances*, 2016, **6**, 44489–44497.
51 Y. Liu, W. Wang, B. Lévy, F. Sun, D.-M. Yan, L. Lu and C. Yang, *ACM Transactions on Graphics (ToG)*, 2009, **28**, 1–17.
52 A. Needleman, *Journal of the Mechanics and Physics of Solids*, 1990, **38**, 289–324.
53 V. Tvergaard and J. W. Hutchinson, *Journal of the Mechanics and Physics of Solids*, 1992, **40**, 1377–1397.
54 A. Needleman, *Journal of Applied Mechanics*, 1987, **54**, 525–531.
55 D. S. Dugdale, *Journal of the Mechanics and Physics of Solids*, 1960, **8**, 100–104.
56 K. Y. Volokh, *Communications in Numerical Methods in Engineering*, 2004, **20**, 845–856.
57 G. I. Barenblatt, *Journal of Applied Mathematics and Mechanics*, 1959, **23**, 622–636.
58 G. I. Barenblatt *et al.*, *Advances in applied mechanics*, 1962, **7**, 55–129.

59 J. R. Rice and J.-S. Wang, *Materials Science and Engineering: A*, 1989, **107**, 23–40.
60 S. Plimpton, *Journal of computational physics*, 1995, **117**, 1–19.
61 D. W. Brenner, O. A. Shenderova, J. A. Harrison, S. J. Stuart, B. Ni and S. B. Sinnott, *Journal of Physics: Condensed Matter*, 2002, **14**, 783.
62 L. Pastewka, P. Pou, R. Pérez, P. Gumbsch and M. Moseler, *Physical Review B*, 2008, **78**, 161402.
63 L. Pastewka, M. Mrovec, M. Moseler and P. Gumbsch, *MRS bulletin*, 2012, **37**, 493–503.
64 L. Pastewka, A. Klemenz, P. Gumbsch and M. Moseler, *Physical Review B*, 2013, **87**, 205410.
65 A. Klemenz, L. Pastewka, S. G. Balakrishna, A. Caron, R. Bennewitz and M. Moseler, *Nano letters*, 2014, **14**, 7145–7152.
66 M. S. Elapolu and A. Tabarraei, *The Journal of Physical Chemistry C*, 2021.
67 E. B. Tadmor and R. E. Miller, *Modeling materials: continuum, atomistic and multiscale techniques*, Cambridge University Press, 2011.
68 N. C. Admal and E. B. Tadmor, *Journal of elasticity*, 2010, **100**, 63–143.
69 J. A. Zimmerman, E. B. WebbIII, J. Hoyt, R. E. Jones, P. Klein and D. J. Bammann, *Modelling and simulation in materials science and engineering*, 2004, **12**, S319.
70 A. Hillerborg, M. Modéer and P.-E. Petersson, *Cement and concrete research*, 1976, **6**, 773–781.
71 M. I. R. Shishir and A. Tabarraei, ASME International Mechanical Engineering Congress and Exposition, 2020, p. V012T12A028.